Clays and Clay Minerals, Vol. 59, No. 2, 176–188, 2011.

APPLICATION OF ELECTRON ENERGY-LOSS SPECTROSCOPY (EELS) AND ENERGY-FILTERED TRANSMISSION ELECTRON MICROSCOPY (EFTEM) TO THE STUDY OF MINERAL TRANSFORMATION ASSOCIATED WITH MICROBIAL Fe-REDUCTION OF MAGNETITE

JINWOOK KIM[1,*] AND HAILIANG DONG[2,3,†]

[1] Department of Earth System Sciences, Yonsei University, Seoul, Korea
[2] Geomicrobiology Laboratory, State Key Laboratory of Geological Processes and Mineral Resources, China University of Geosciences, Beijing, 100083, China
[3] Department of Geology, Miami University, Oxford, OH 45056, USA

Abstract—Electron energy-loss spectroscopy (EELS), energy-filtered transmission electron microscopy (EFTEM), and high-resolution transmission electron microscopy (HRTEM) have been applied in mineralogy and materials research to determine the oxidation states of various metals at high spatial resolution. Such information is critical in understanding the kinetics and mechanisms of mineral–microbe interactions. To date, the aforementioned techniques have not been applied widely in the study of such interactions. In the present study, the three techniques above were employed to investigate mineral transformations associated with microbial Fe(III) reduction in magnetite. *Shewanella putrefaciens* strain CN32, a dissimilatory metal-reducing bacterium, was incubated with magnetite as the sole electron acceptor and lactate as the electron donor for 14 days under anoxic conditions in bicarbonate buffer. The extent of bioreduction was determined by wet chemistry and mineral solids were investigated by HRTEM, EFTEM, and EELS. Magnetite was partially reduced and biogenic siderite formed. The elemental maps of Fe, O, and C and red-green-blue (RGB) composite map for residual magnetite and newly formed siderite were contrasted by the EFTEM technique. The HRTEM revealed nm-sized magnetite crystals coating bacterial cells. The Fe oxidation state in residual magnetite and biogenic siderite was determined using the EELS technique (the integral ratio of L_3 to L_2). The integral ratio of L_3 to L_2 for magnetite (6.29) and siderite (2.71) corresponded to 71% of Fe(III) in magnetite, and 24% of Fe(III) in siderite, respectively. A chemical shift (~1.9 eV) in the Fe-L_3 edge of magnetite and siderite indicated a difference in the oxidation state of Fe between these two minerals. Furthermore, the EELS images of magnetite (709 eV) and siderite (707 eV) were extracted from the electron energy-loss spectra collected, ranging from 675 to 755 eV, displaying different oxidation states of Fe in the magnetite and siderite phases. The results demonstrate that EELS is a powerful technique for studying the Fe oxidation-state change as a result of microbial interaction with Fe-containing minerals.

Key Words—Electron Energy-loss Spectroscopy (EELS), Energy-filtered Transmission Electron Microscopy (EFTEM), Magnetite, *Shewanella putrefaciens*, Siderite.

INTRODUCTION

Biogeochemical mineral transformations associated with microbial Fe(III) reduction have been of great interest because previous studies demonstrated the significant role of Fe in controlling redox balance and carbon cycling in sediments (Nealson and Saffarini, 1994) and the implications of biological redox processes for fate and transport of multivalent toxic metals and radionuclides in natural environments (Nealson and Little, 1997; Lovley *et al.*, 1995). Metal-reducing bacteria are capable of reducing structural Fe(III) in minerals and precipitating amorphous or crystalline mineral phases (Fredrickson *et al.*, 1998; Liu *et al.*, 2001; Kukkadapu *et al.*, 2001; Kostka and Nealson, 1995; Dong *et al.*, 2000; Kostka *et al.*, 1999; Kim *et al.*, 2004; Dong *et al.*, 2009). The extent and rate of bioreduction depends on a number of factors, including mineral surface area (Roden and Zachara, 1996), sorption capacity of mineral surfaces for Fe^{2+} (Liu *et al.*, 2001; Jaisi *et al.*, 2007), the presence or absence of chelating agents (*i.e.* AQDS), complexing agents (Fredrickson *et al.*, 1998), and type of microorganisms (Dong *et al.*, 2009 and references therein). Certain types of bacteria can enhance bioreduction *via* production of their own electron-shuttling compounds such as quinones (Newman and Kolter, 2000), chemotaxis (Childers *et al.*, 2002), or by using naturally present electron-shuttling compounds (Nevin and Lovely, 2002). Microbial reduction of Fe(III) in minerals often results in mineral dissolution and neoformation of biogenic minerals (Kim *et al.*, 2004; Li *et al.*, 2004; Tazaki and Asada, 2001; Dong *et al.*, 2009 and references therein). The studies listed have demonstrated collectively that major structural changes can take place when minerals

* E-mail addresses:
* Jinwook@yonsei.ac.kr
† dongh@muohio.edu
DOI: 10.1346/CCMN.2011.0590206

interact with microbes. Few attempts have been made, however, to investigate the microbe-mediated mineral transformations at the micro- and nano-scale. This level of investigation is essential to reveal the interaction mechanisms and to establish the biogenicity of residual and neoformed minerals (Benzerara and Menguy, 2009). Pilot studies on the application of EELS and EFTEM techniques to biomineralization studies (Daulton *et al.*, 2002) revealed important information on the pathways of microbially induced mineralization (Buatier *et al.*, 2004) and the spatial variation of the oxidation state of chromium when it was reduced by metal-reducing bacteria (Daulton *et al.*, 2002). Precipitates encrusting bacterial cells exhibited a reduced form of Cr (Cr^{3+}) (Daulton *et al.*, 2007), suggesting that the cell-envelope region represents an active interaction zone. Such insights were made possible by the EELS and EFTEM techniques which are capable of measuring mineral oxidation state at the nano-scale.

The purpose of the present study was, therefore, to demonstrate the application of EELS and EFTEM techniques to the characterization of the biogeochemical transformation of magnetite accompanying microbial Fe reduction. Dong *et al.* (2000) demonstrated that *Shewanella putrefaciens* strain CN32, a dissimilatory metal-reducing bacterium, could cause the dissolution of magnetite and the formation of siderite under natural conditions. However, that study did not employ EFTEM and EELS techniques to investigate mineral transformations. The research described here is, therefore, a continuation of the Dong *et al.* (2000) study, using the EELS and EFTEM techniques to elucidate the changes in oxidation state of Fe in newly precipitated minerals as a result of microbial reduction of Fe(III) in magnetite. The oxidation state of Fe was determined, and the three-window elemental mapping technique and EELS-spectrum image analysis were performed.

MATERIALS AND METHODS

Bacterial culture and reduction experiment

Shewanella putrefaciens CN32 cells were grown in aerobic tryptic soy broth (TSB), washed with bicarbonate buffer to remove TSB, and purged with anoxic N_2:CO_2 gas (80:20). Cells were incubated with lactate as the electron donor and Fe(III) in magnetite as the sole electron acceptor for 14 days in bicarbonate buffer or piperazine-N,N′-bis(2-ethanesulfonic acid) (PIPES) buffer (Fredrickson *et al.*, 1998). The final cell concentration in the experimental tubes was determined to be $2-3 \times 10^8$ mL^{-1}, as determined by acridine orange direct count (AODC) and colony-forming units (CFU). Any changes in cell concentration during the bioreduction experiment were not recorded. In selected experiments, soluble phosphate in the form of NaH_2PO_4 was added. The magnetite used in the present study was produced biogenically from microbial reduction of ferric hydrous oxide (Fredrickson *et al.*, 1998) after removal of cell debris and any other mineral phases. The entire removal procedure involved extraction of Fe(II) using 1 M Na acetate (pH 4.5−5), removal of residual cells and cell debris with 10% NaOH, followed by two washes in 0.1 M Na perchlorate (Dong *et al.*, 2000). The entire procedure was conducted in anaerobic water under an anoxic atmosphere. The cleaned magnetite was untainted with any other Fe mineral phases, as verified by Mössbauer spectroscopy (Dong *et al.*, 2000). Controls consisted of solutions with anaerobic bicarbonate buffer instead of CN32 cell suspensions. Details of the procedure for the bioreduction experiment are given elsewhere (Dong *et al.*, 2000).

Ferrozine assay

The extent of microbial reduction of Fe(III) in the magnetite structure was monitored by measuring Fe(II) production over time. After 14 days, 0.1 mL of cell−mineral suspension, sampled using a sterile syringe, was added to a plastic tube which already contained 0.1 mL of 1 N Ultrex HCl (referred to as 0.5 N HCl extraction because the final concentration of HCl was 0.5 N). The cell−mineral suspension was allowed to stand in HCl for 24 h before measuring the Fe(II) concentration. The 0.5 N HCl extraction, though effective at extracting microbially produced Fe(II), including the adsorbed form, and Fe(II) in many biogenic solids, has been shown to be ineffective at extracting all Fe(II) from the magnetite structure (Fredrickson *et al.*, 1998; Zachara *et al.*, 1998) and from silicates (Jaisi *et al.*, 2007; Anastacio *et al.*, 2008). The amount of Fe(II) measured may, therefore, underrepresent the true extent of bioreduction. Furthermore, this wet chemical extraction provides no information on the spatial distribution of Fe(II) and Fe(III) in relation to microbial activity. For this reason, the same samples were characterized by HRTEM in order to image the cell−mineral associations and by EELS to determine the Fe(II)/Fe(III) ratios at a high spatial resolution.

HRTEM

High-resolution TEM characterization was performed to observe cell−mineral associations and to study the mineral-transformation processes at the micro- to nano-scales. The lattice-fringe images were obtained using a JEOL JEM-3010 transmission electron microscope (JEOL USA, Peabody, Massachusetts) operating at 300 keV with a LaB_6 filament in the Electron Microscopy Center at the Naval Research Laboratory − SSC, Mississippi, USA. Specimens were impregnated with nanoplast resin (Leppard, 1996) and sliced to a thickness of 70 nm using a Leica Ultracut UCT microtome (Kim *et al.*, 2003, 2004). The advantage of using hydrophilic Nanoplast resin in the present study is that solvent exchange (methanol/water exchange), necessary for the L.R. White resin-impregnation

technique (Kim *et al.*, 1995), is not required. The Nanoplast resin contains no reducing agent and does not alter the oxidation state of any redox-sensitive elements (Kim *et al.*, 2003, 2004).

EELS

The main capability of the EELS technique is derived from the fact that it probes primary rather than secondary events [*e.g.* energy dispersive spectrum (EDS) or Auger electrons]. Primary events are highly localized and, as such, no peripheral fluorescence or interactions occur. The EELS signals, therefore, result from the direct interactions between the incident beam and the specimen electrons. The energy loss of inelastically scattered electrons is measured which is related to the electronic structure and oxidation states of transition metals of the specimen (Leapman *et al.*, 1982; Paterson and Krivanek, 1990; Garvie *et al.*, 1994, van Aken *et al.*, 1998; van Aken and Liebscher, 2002; Daulton *et al.*, 2002; Zhang *et al.*, 2010). Determination of the oxidation state of Fe by the EELS technique has been developed in the past decade, since the first findings of changes in valence-dependent white-line intensity ratio of L_3/L_2 adsorption edges (Leapman *et al.*, 1982), and valence-induced difference of Fe L_{23} energy loss near edge structure (Taftø and Krivanek, 1982). Van Aken *et al.* (1998) and van Aken and Liebscher (2002) developed a universal curve as a function of the integral white-line intensity ratio of L_3/L_2 *vs.* ferric Fe concentration using natural mineral samples and mineral solid solutions. The oxidation-state changes in Cr associated with metal-reducing bacteria have also been measured by comparing the L_3/L_2 integrated peak ratio of Cr standards (Daulton *et al.*, 2002). Tazaki and Asada (2007) reported the distribution of mercury in clay minerals associated with bacterial activity at the nano-scale using the EFTEM technique.

The EELS data were obtained using a JEOL JEM-2010 transmission electron microscope operating at 200 keV with a LaB_6 filament in the Electron Microscopy Center at Gatan, Inc. (Pleasanton, California, USA). The instrument was equipped with a Gatan imaging filter (GIF200) capable of EELS. The following conditions were used during collection of EELS spectra: convergence angle = 5 mrad, collection angle = 2 mrad, 2.0 mm entrance aperture, energy dispersion of 0.6 eV/pixel (0.6 eV/pixel × 1024 pixels = 614.4 eV in total), and energy resolution of 1 eV. Low-loss spectra were acquired with an integration time of 0.1 s (15 spectra summed) and L-edge spectra with an integration time between 0.1 and 1.0 s (between 90 and 200 spectra summed). Spectra were collected in the diffraction mode of the TEM (*i.e.* image coupling to the EELS spectrometer) and were corrected for dark current and channel-to-channel gain variation of the charge-coupled device (CCD) detector. The Fe-L edge background was subtracted from L-edge spectra using a standard inverse power law and plural inelastic scattering was removed by Fourier deconvolution methods. The statistical measurements of the integral ratio of L_{23} edges were made using the Gatan *DigitalMicrograph* software in which the method was applied to determine the statistically optimum signal-window parameters. In general, the signal window starts at the steepest intensity increase such as 702.5 eV for siderite L_3 (see Figure 6) and the signal-integration window should always be narrower than the background region. The signal-integration windows of 702.5−714.5 eV (L_3) and 717.5−725 eV (L_2) for magnetite, and 705.5−715 eV (L_3) and 717.5−725 eV (L_2) for siderite were used to calculate the integral intensity ratio of L_3/L_2 for each mineral. The integrated background intensity under the Fe-L_2 and Fe-L_3 edges was subtracted from the integrated-signal intensity at the Fe-L_2 and Fe-L_3 edge positions. From these measured values, the ratio of Fe-L_3 to Fe-L_2 was determined to estimate the Fe oxidation state using the universal curve, *i.e.* the integral ratio of L_3/L_2, *i.e.* ferric Fe concentration as determined by van Aken *et al.* (1998). Analysis of a range of Fe-oxidation state standards is important in order to determine any unknown with certainty. The integral intensity ratio of L_3/L_2 for well characterized Fe(III) standards, *e.g.* annite (11% of Fe(III), L_3/L_2 = 1.92) from Pikes Peak (Dyar *et al.*, 1986) and muscovite OK-8 (41% of Fe(III), L_3/L_2 = 3.31) from Oquossoc Quadrangle, Maine, (Dyar, pers. comm.) were tested, therefore, resulting in a good match (Figure 1) with the measurements by van Aken *et al.* (1998). Furthermore, EELS-spectrum image analysis, which contained both spatial and dispersion (energy-loss) information, was performed. The EELS spectrum image is capable of resolving spectral information at the sub-nanometer scale (small-energy window), as such a small energy shift due to the Fe-oxidation state (chemical shift) is visualized efficiently in an oxidation-state map. Aligned EELS spectrum images of magnetite and siderite at electron energy loss from 675 to 755 eV were collected with a step size of ΔE = 1 eV, for example. Magnetite and siderite L_{23} spectra were extracted at 709 and 707 eV, respectively, to obtain the Fe oxidation-state image. The EELS spectra collected for the spectrum image were aligned by means of a batch-collection and processing technique (Hunt and Williams, 1991) and then multiple least-squares (MLS) fitting (Leapman and Sywt, 1988); background modeling by a standard inverse power law was applied using the Gatan *DigitalMicrograph* software.

Energy-filtered TEM (EFTEM)

The EFTEM enhances contrast in images and diffraction patterns by removing inelastically scattered electrons which produce background. An energy filter can produce images of a narrow range of energy loss, which can be used to create elemental/chemical maps. In

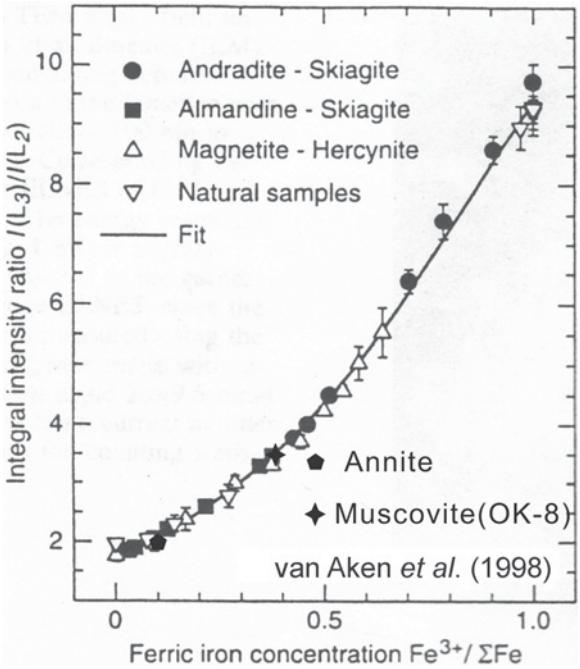

Figure 1. The integral intensity ratio of L_3/L_2 for Fe(III) oxidation state standards, *e.g.* annite (11% of Fe(III), L_3/L_2 = 1.92) from Pikes Peak (Dyar and Burns, 1986) and muscovite OK-8 (41% of Fe(III), L_3/L_2 = 3.31) from Oquossoc Quadrangle, Maine, (Dyar, pers. Comm.) resulting in an excellent match with measurements by van Aken *et al.* (1998).

particular, ferrous/ferric Fe distribution can be mapped using the differences in EELS spectra and the chemical shift of the Fe L_{23} ionization edges of Fe^{2+} and Fe^{3+} (Golla and Putnis, 2001). Chemical shift occurs when redistribution of valence charge alters the potential energy of initial core states which causes edge thresholds to shift.

Elemental distribution of Fe, O, and C in magnetite and siderite was determined by the EFTEM three-window mapping method which uses two pre-edge images to compute a background contribution to the post-edge images. The post-edge image contains element-specific core-loss signals and background from low-energy excitation, and two pre-edge images are used to characterize the background signal. Subtraction of the computed background component (electrons that contain no information on structure/valence *etc*.) by power-law extrapolation from the post edge image isolates the true edge signal, and, as such, the background component no longer contributes to the image. Optimal pre-edge window placement follows the general rule, *e.g.* the high-energy side of the pre-edge window should be as close to the analyzing edge as possible, typically 5 eV ahead of the threshold energy. The pre-edge window width may be in the range between 10% and 30% edge energy, and should be larger than the signal integration window (post-edge window). Elemental images of the Fe-L_{23} edge at 708 eV, the O-K edge at 532 eV, and the C-K edge at 284 eV were collected by the three-window method. A color was assigned to each element, *e.g.* blue – carbon, green – oxygen, and red – iron, and then three color layers were superimposed to create a red-green-blue (RGB) composite elemental map.

RESULTS

Microbial Fe-reduction of magnetite

The 0.5 N HCl extraction includes microbially reduced Fe(II) and Fe(II) associated with the original magnetite sample. Nevertheless, the Fe(II) concentration was 1.5 to 1.7 times greater in the bioreduced sample at the end of 14 days than in the uninoculated control, indicating extensive biological reduction in various types of medium (Figure 2).

HRTEM

Transmission electron microscopy observations of ultra-thin sections of bacteria–mineral solids from the 7-day time point showed aggregations of nanocrystalline magnetite around the surface of *Shewanella putrefaciens* strain CN32 (Figure 3a). At the end of incubation (14 days), coarse grains (larger and thicker in size and darker in contrast than the magnetite grains) were observed inside magnetite aggregates (Figure 3b) in

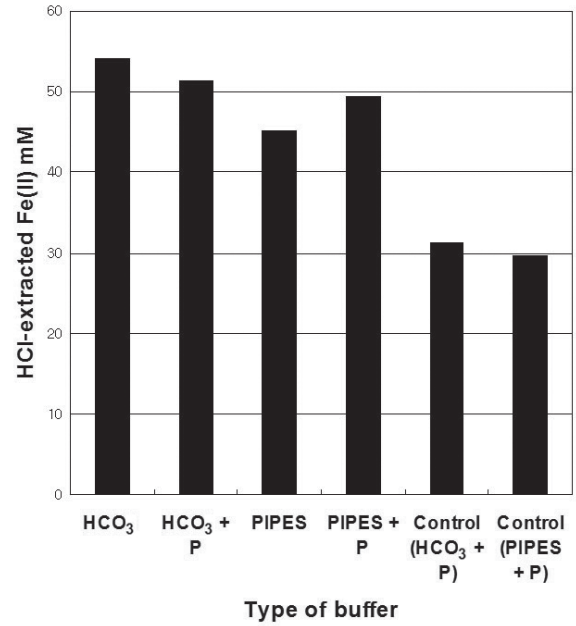

Figure 2. HCl-extracted Fe(II) at the end of 14 days of incubation. The concentration of the HCl-extracted Fe(II), as measured by ferrozine assay, increased with time, and at the end of the incubation experiment, the Fe(II) concentration was 1.5 to 1.7 times greater in the bioreduced sample than in the uninoculated control regardless of buffer type. The letter 'P' stands for soluble phosphate.

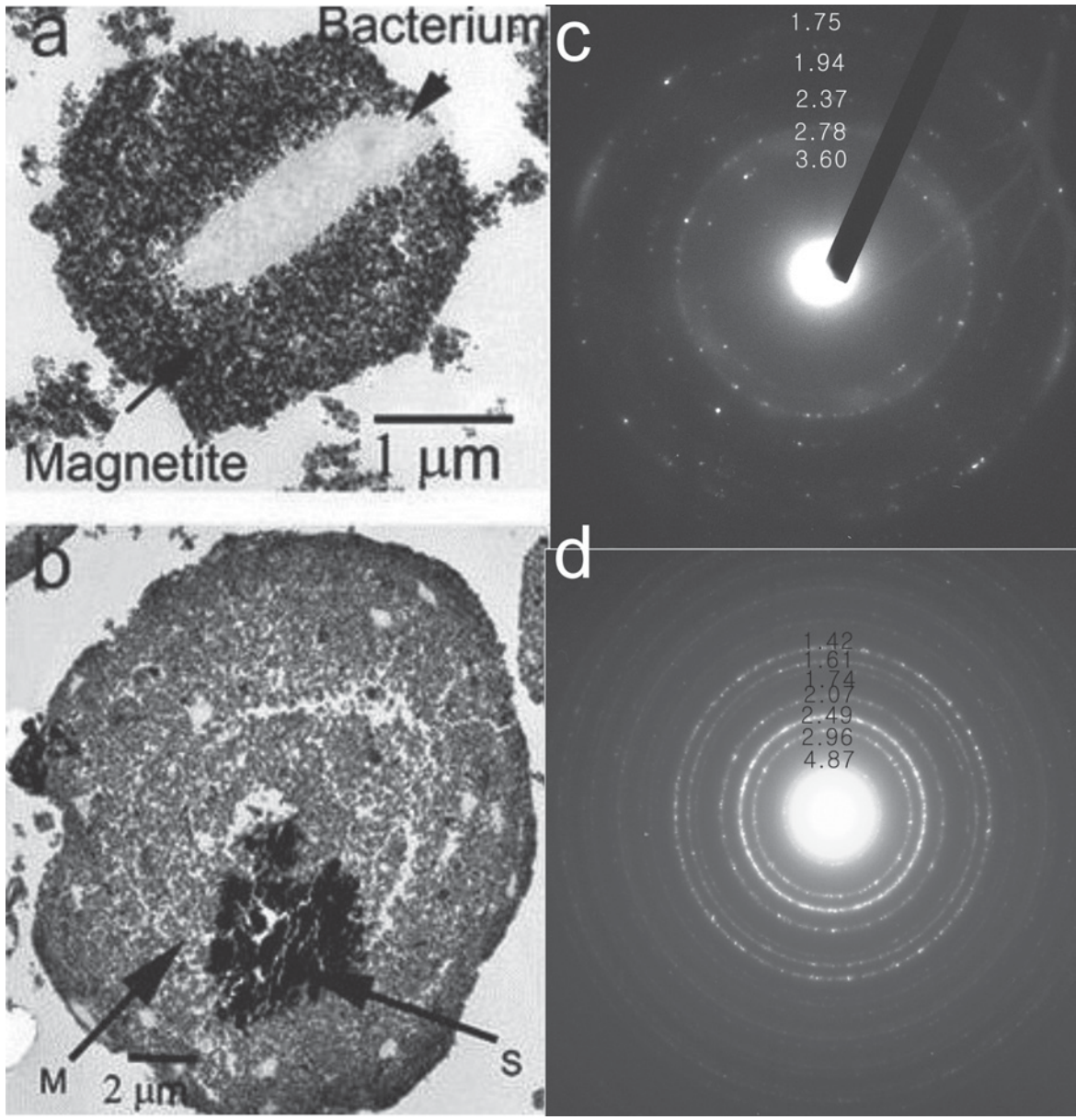

Figure 3. Bright-field TEM images of (a) magnetite which coated the bacterial cell, and (b) siderite (S) inside a thick coating of magnetite (M) particles. Selected area electron diffraction (SAED) patterns of (c) siderite and (d) bulk magnetite (away from the magnetite–siderite interface).

locations previously occupied by bacteria (Figure 3a). After the 14 days, the bacteria had apparently lysed and decomposed, leaving space for the coarse grains to precipitate. Some empty holes with the same size and shape as bacterial cells were preserved but no particles filled the space (data not shown). Selected area electron diffraction (SAED) patterns of the coarse grains (S) showed strong reflections with *d* values of 3.60, 2.78, 2.37, 1.94, and 1.75 Å, consistent with siderite (Figure 3c, Table 1). The diffuse rings may be due to inclusion of many small particles. The *d* values of 4.87, 2.96, 2.49, 2.07, 1.74, 1.61, and 1.42 Å were measured for residual magnetite (Figure 3d, Table 1). The measured SAED data for magnetite and siderite were summarized and compared with their respective standards (Table 1).

EELS

The area of interest in the bio-reduced magnetite sample was selected based on the optimum sample thickness to perform EELS and EFTEM analyses as described below. The zero-loss image (image taken at

Table 1. Electron-diffraction data for magnetite and siderite.

Standard magnetite* (Å)	Observed magnetite (Å)	Standard siderite** (Å)	Observed siderite (Å)
4.850 (8)†	4.87	3.593 (25)	3.60
2.967 (30)	2.96	2.795 (100)	2.78
2.532 (100)	2.49	2.346 (20)	2.37
2.424 (8)		2.134 (20)	
2.099 (20)	2.07	1.965 (20)	1.94
1.715 (10)	1.74	1.797 (12)	
1.616 (30)	1.61	1.738 (30)	1.75
1.485 (40)	1.42	1.732 (35)	

* JCPDS card 19-629; ** JCPDS card 29-696
†: Denotes relative XRD intensity

$\Delta E = 0$ eV), capable of improving resolution by eliminating chromatic blurring (Figure 4), displays two dominant phases, fine magnetite and coarse siderite particles with a strong image contrast. Again, the siderite clusters appeared to have filled in the open spaces and the void shown in Figure 3 top suggests that these open spaces were previously occupied by bacterial cells.

EELS quantification. The entire EELS spectrum of a siderite-dominant area, including the zero-loss (elastic) peak, the low-loss region (up to 50 eV), and the core-loss region (160−800 eV) was collected (Figure 5). The background (red line) was subtracted, resulting in intensified core-loss signals (green). In order to obtain EELS data corresponding to single scattering events, the specimen needs to be suitably thin (thickness < λ, where λ is the mean free path for inelastic scattering). The relative sample thickness (thickness/λ = 0.33) of the region of interest was measured using the log-ratio method (thickness/$\lambda = -\ln (I_0/I_t)$, where I_0 is the integrated zero-loss intensity and I_t is the total integrated intensity) using the Gatan *DigitalMicrograph* software. The Fe-L_{23} edge at 708 eV, the O-K edge at 532 eV, and the C-K edge at 284 eV were identified by edge threshold energy (steepest rise), edge shape, and *DigitalMicrograph* edge ID (Figure 5).

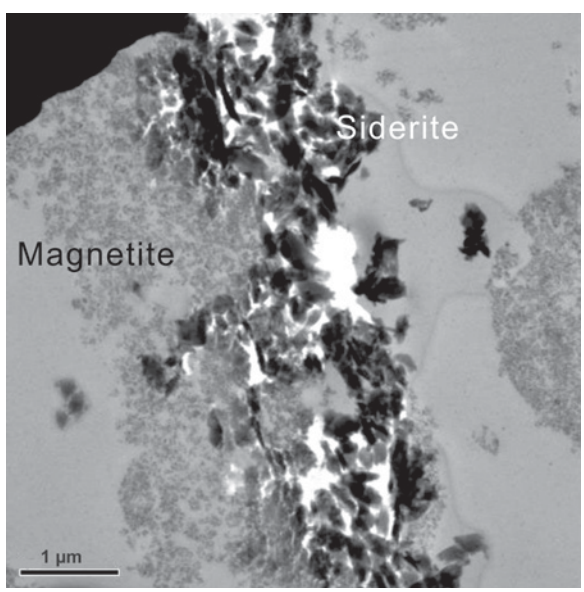

Figure 4. Zero-loss image (image taken at E = 0 eV) which improves resolution by eliminating chromatic blurring.

Fe-oxidation state. The magnetite and siderite were investigated using the EELS technique to determine the Fe-oxidation state in each mineral. The background was extracted by the standard inverse power law. A chemical shift (~1.9 eV) of the Fe-L_3 edges of magnetite and siderite was measured in the EELS spectrum (Figure 6). A total count of L_3 and L_2 edges and calculated integral ratio of L_3/L_2 for bulk magnetite and siderite are summarized in Table 2. The integral ratios of L_3 to L_2 for siderite (2.71) and the bulk magnetite (unreduced, away from the siderite interface) (6.29), calculated by statistical analysis in the *DigitalMicograph* software, corresponded to ~24% and ~71% of Fe(III), respectively, based on the calibration curve (see Figure 1) of van Aken *et al.* (1998). The oxidation state referred to the percentage of Fe(III) in the total Fe for that phase.

Table 2. Total counts of L_3 and L_2 edges and calculated integral ratio of L_3/L_2 for magnetite and siderite (unit: 10^3 photodiode counts)

	Magnetite	Siderite
L_3	4913.54	9537.75
L_3 background	3627.15	7850.62
L_3 (background removed)	1286.39	1687.13
L_2	3218.45	6047.21
L_2 background	3014.04	5423.89
L_2 (background removed)	204.41	623.32
L_3/L_2	6.29	2.71

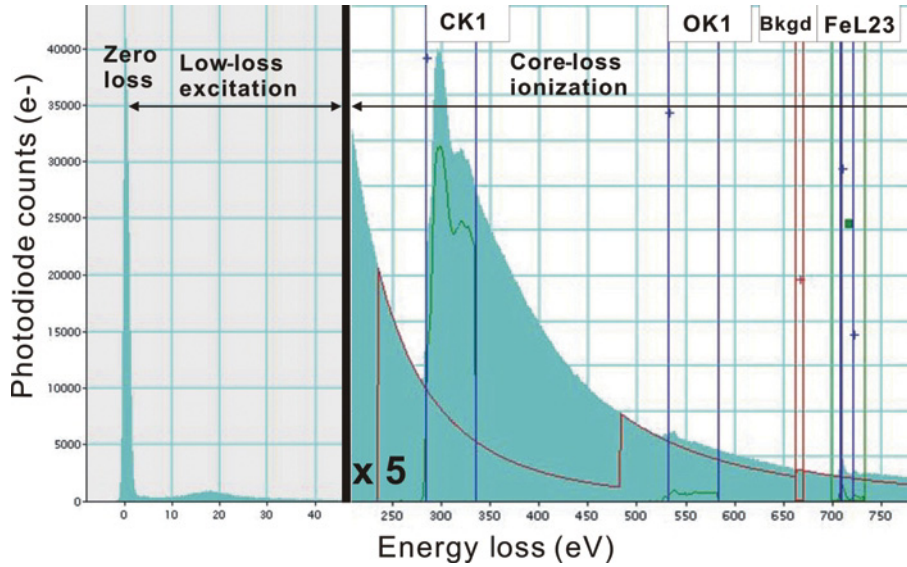

Figure 5. EELS spectrum including peaks in the zero-loss (elastic), low-loss (up to 50 eV), and core-loss (160–800 eV) regions of the siderite-dominant area.

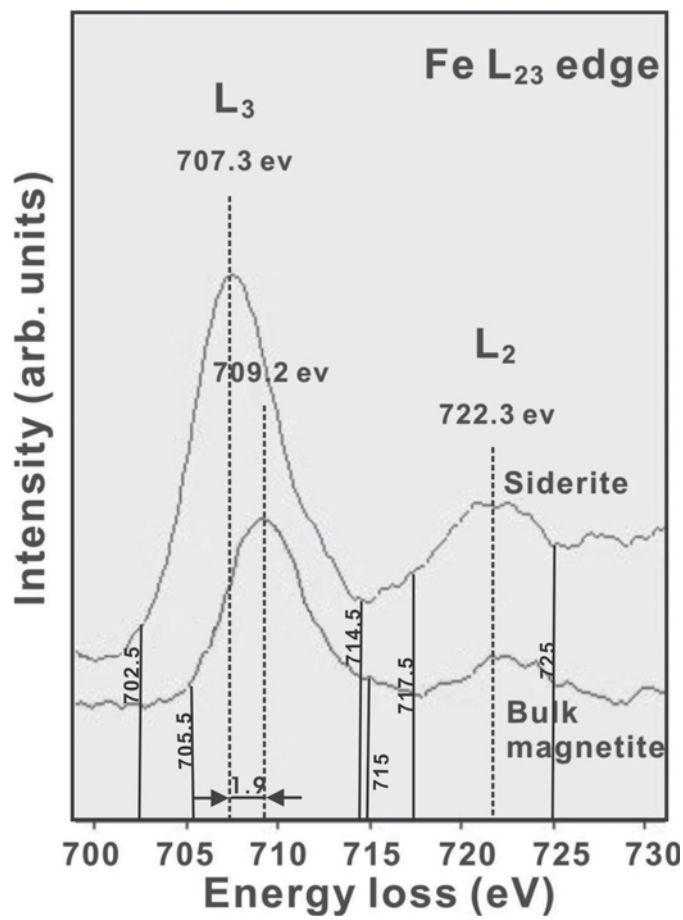

Figure 6. EELS spectra of magnetite and siderite to determine the Fe oxidation state in each mineral. The background was extracted by the standard inverse power law. An energy shift (~1.9 eV) of Fe-L_3 edges of magnetite and siderite was measured. The signal-integration windows of 702.5–714.5 eV (L_3) and 717.5–725 eV (L_2) for magnetite, and 705.5–715 eV (L_3) and 717.5–725 eV (L_2) for siderite were used to calculate the integral intensity ratio of L_3/L_2 for each mineral.

EELS spectrum image. The spectrum image of the energy-loss region between 675 and 755 eV with 1 eV energy-loss resolution was extracted from the EELS signal and then aligned as shown in Figure 7a. The contrast changes clearly in the image extracted from the Fe(III)-dominant magnetite L_{23} spectrum (at 709 eV) (Figure 7b) and Fe(II)-dominant siderite L_{23} spectrum (at 707 eV) (Figure 7c). The changes in contrast are associated with EELS signals extracted from the specific energy loss of the element in the mineral (*e.g.* Fe in magnetite and siderite) and the chemical shift resulted from the variance in oxidation states. The magnetite (M) particles are highlighted in Figure 7b while the siderite particles (S) are efficiently resolved in Figure 7c.

EFTEM image. To further determine the distribution of elemental composition in siderite and magnetite at the nano-scale, C, O, and Fe elemental mapping conditions for the EFTEM three-window method were summarized in Table 3. These conditions were based on the optimal background and signal extraction window placement described in the methods section. The computed background of pre-edge1 and pre-edge2 for each element by the power-law extrapolation was subtracted from a post-edge image, resulting in a core-loss signal image (Figure 8). The RGB elemental composite maps, using the three-window elemental maps, were created using the *DigitalMicograph* software (Figure 9).

DISCUSSION

Application of EELS and EFTEM to biomineralization studies

The EELS technique has been applied in mineralogy and materials research to determine the oxidation states of Fe (van Aken *et al.*, 1999; Golla and Putnis, 2001; van Aken and Liebscher, 2002). The potential application of this technique in studying microbial metal reduction has been recognized by several researchers (Daulton *et al.*, 2002; Middleton *et al.*, 2003; Buatier *et al.*, 2004). Compared to other techniques such as Mössbauer spectroscopy, EELS has the advantage of measuring oxidation states at a high spatial resolution. The minimum level of Fe detectable by EELS is 2−3% and the smallest area that can be focused by TEM with a LaB6 filament is 1 nm × 1 nm (in the present study). Another major advantage of EELS is that the textural relationship between minerals is maintained, something that is impossible in Mössbauer spectroscopy. One prerequisite for simultaneous measurement of Fe(II) and Fe(III) is that the energy resolution of the EELS

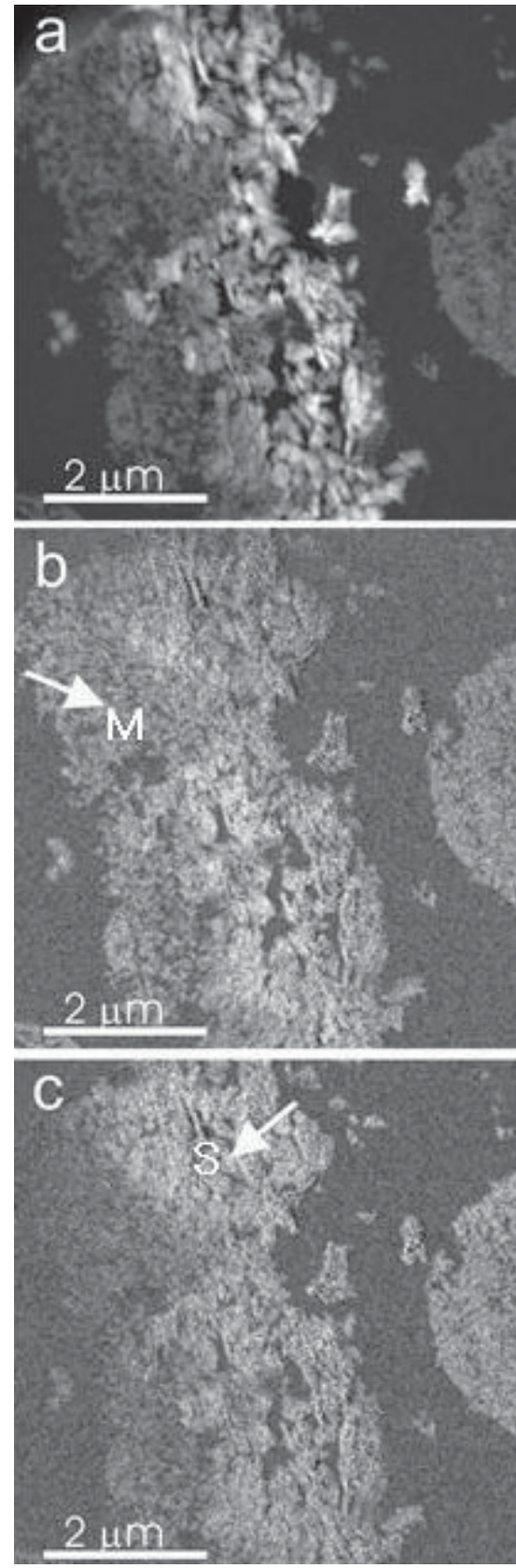

Figure 7. The spectral image of (a) aligned energy-loss region between 675 and 755 eV with 1 eV energy-loss dimension, (b) the Fe(III)-dominant magnetite (M) L_{23} spectrum at 709 eV, and (c) Fe(II)-dominant siderite (S) L_{23} spectrum at 707 eV.

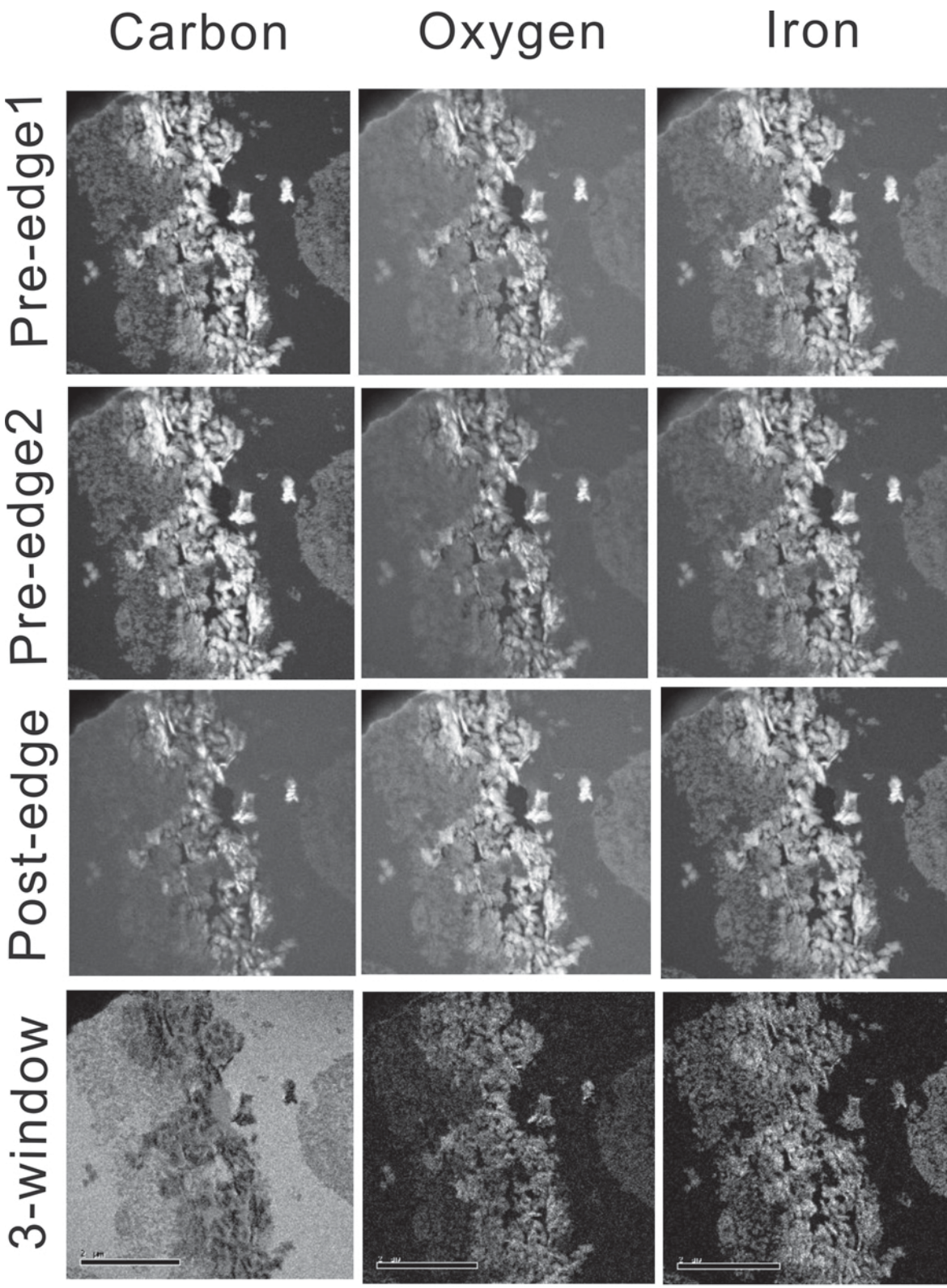

Figure 8. Elemental maps of C, Fe, and O at the magnetite–siderite interface by three-window elemental maps.

Table 3. Elemental mapping setup.

Element	Edge	Energy (eV)	Pre-edge1 Δ (eV)	Pre-edge2 Δ (eV)	Post-edge Δ (eV)	Slit width (eV)
C	K	284	49	19	30	30
O	K	532	35	15	20	20
Fe	L_{23}	708	34	18	26	26

instrument (1 eV in the present case) has to be greater than the energy shift of the L3 peak caused by the Fe oxidation state change (*i.e.* from Fe^{2+} to Fe^{3+} or *vice versa*, Figure 6). If this condition is satisfied, virtually any metals with multiple oxidation states can be measured, assuming that an adequate number of standards is available for calibration. Furthermore, EELS spectrum images extracted from specific energy-loss of elements, *e.g.* 709 eV (Fe in magnetite) and 707 eV (Fe in siderite) corresponding to the chemical shift due to the various Fe-oxidation states, can visualize efficiently the changes in oxidation state by image contrast (Figure 7). The EELS signals extracted with 1.9 eV chemical shift for each Fe-oxidation state would be strong enough to display the images with contrast. Furthermore, the elemental maps at the nanometer scale were created by the EFTEM technique (Golla and Putnis, 2001; and the present study). The main advantage of processing elemental maps using EFTEM is that each element signal was extracted from the high spatial resolution of EELS (energy loss characteristic of an atomic core level) such as the Fe-L_{23} edge at 708 eV, the O-K edge at 532 eV, and the C-K edge at 284 eV, which allows the user to create high-resolution elemental maps with excellent chemical accuracy as shown in Figures 8 and 9. The three-window method in the present study effectively removed background signals of low-energy excitation for the high-resolution image, compared with the two-window method (not shown). This feature is especially attractive to studies of microbe–mineral systems, where microbial reduction of metals may be heterogeneous horizontally (over the cell membrane) and/or vertically (from the outer membrane, periplasm, to cytoplasm). Microbe–mineral interactions may enrich or deplete certain elements and create non-stoichiometric compositions (Elliott, 2002; Tazaki and Asada, 2001; Li *et al.*, 2004). The spectrum image may not be feasible when the chemical shift associated with the oxidation states of elements is less than the resolution of electron energy loss, however. Also, the corrections of spectrum artifacts and the drift of spatial and energy coordinates of the spectrum-image should be considered during image processing. In the present study, the *DigitalMicograph* software was capable of correcting the spectra artifact and drifting problem through MLS fitting and background modeling.

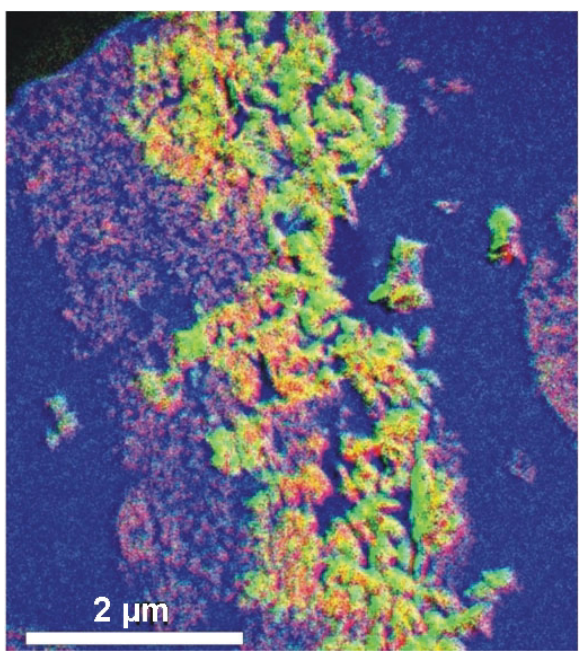

Figure 9. The RGB elemental composite maps (red – iron, blue – carbon, and green – oxygen) using a three-window elemental mapping technique. Because magnetite contains more Fe than siderite, the reddish color corresponds to magnetite and the greenish color corresponds to siderite.

Many applications are possible for using the combined EELS, spectral imaging, and EFTEM to study the biomineralization process. For example, the formation mechanism of magnetosomes (intracellular magnetite crystals inside magnetotactic bacteria) remains to be studied further (Bazylinski and Frankel, 2003), and the EELS technique would be ideal to trace the dynamic change of Fe redox reactions at different stages of magnetosome formation. When coupled with chemical analyses and mineral identification, this type of data could reveal important information on initial Fe uptake mechanism into the cell, subsequent oxidation-state change (reduction or oxidation), and the final mineral phases formed.

Mineral transformations

Multiple lines of evidence have demonstrated that bioreduction of Fe(III) in magnetite produced biogenic siderite. The textural evidence suggests that the interface between magnetite and bacteria (Figure 3a) may represent an active region, where biological reduction

of Fe(III) took place. During the early stage of bioreduction, the magnetite coating may have been sufficiently porous to allow transport of nutrients into the cell and wastes out of the cell, and the bacteria may have remained viable. As the reduction continued and the magnetite coating thickened, the encrusted bacteria may have experienced increased difficulty with respiration. As a result, the bacteria lysed and decomposed, leaving characteristic 'skeletons'; once the 'skeletons' are filled by new minerals, they can be used as biosignatures (Konhauser and Ferris, 1996; Konhauser *et al.*, 2004).

Bacterial decomposition and opening of space, along with reductive dissolution of magnetite, would have allowed precipitation of biogenic siderite when the solution became supersaturated with respect to siderite. The fact that the siderite clusters were located inside the magnetite coatings (Figure 3) and within open spaces (Figure 4) strongly support this mechanism. The siderite clusters did not preserve the size and shape of the bacteria, however (Figures 3, 4), indicating that some repackaging took place during the dissolution of magnetite and precipitation of siderite. The siderite precipitation appeared to be rapid, because no siderite was observed in the day-7 sample (Figure 3a), but abundant siderite clusters were observed in the day-14 sample (Figure 3b). Rapid growth of siderite would have incorporated some cell debris and even some Fe(III) into the structure, accounting for the non-stoichiometric nature of its Fe(II) content, *i.e.* 24% Fe(III) in the siderite structure (Figure 6, Table 2). Three alternative explanations for the excess Fe(III) in the siderite structure are possible. (1) The 24% Fe(III) content in siderite could have been caused by inclusion of a small amount of magnetite in the beam. (2) The electron beam may have induced oxidation of structural Fe(II) to Fe(III), as observed previously (Garvie *et al.*, 1994, 2004). This mechanism is unlikely because the beam-induced oxidation of Fe(II) to Fe(III) typically occurs in H-bearing minerals and is typically related to H loss (Garvie *et al.*, 1994, 2004). (3) The excess Fe(III) could have been in the structure of biogenic minerals, and indeed other biominerals such as apatite (Elliott, 2002), nontronite (Li *et al.*, 2004), and halloysite (Tazaki and Asada, 2001) have exhibited non-stoichoimetric structure and composition. A previous study observed that biogenic halloysite can be non-stoichiometric because of a combination of random stacking of structural layers and incorporation of abundant organic material into the halloysite interlayer (Tazaki and Asada, 2001). Incorporation of organic material into the siderite structure would provide a mechanism to balance the charge caused by the excess Fe(III).

Mineral non-stoichoimetry might result from (1) preferential removal of certain elements from the mineral structure during microbial dissolution leaving the original structure largely unchanged; (2) kinetic effects of mineral nucleation and growth (*e.g.* local deviation from supersaturation); or (3) incorporation of organic molecules into mineral structure. Incorporation of organic molecules can result in the disappearance of structural regularity in the smectite structure and the absence of the smectite 001 peaks (Eberl *et al.*, 1998). Biological activity can also introduce kinetic effects, and many different observations of diverse organisms have been made in which mineral precipitation appears to be out of equilibrium (Weiner and Dove, 2003). Because bacteria are small particles possessing a large surface area with multiple reactive sites, they promote mineral development by reducing the total free energy required for precipitation. Indeed, minerals are often observed on cell surfaces, and many of them are poorly crystalline or of local order only (Konhouser, 1998).

ACKNOWLEDGMENTS

The present work was supported by grants from NRF of Korea (2009-0085989), the US Department of Energy (DE-FG02-07ER64369 and DE-SC0005333), the 111 projects of China (Nos B07011), the National Basic Research Program of China (2011CB808800), and the National Science Foundation of China (41030211). The authors are grateful to three anonymous reviewers and to the Associate Editor, L.B. Williams, whose comments significantly improved the quality of the manuscript.

REFERENCES

Anastacio, A.S., Harris, B., Yoo, H.-I., Fabris, J.D., and Stucki, J.W. (2008) Limitations of the ferrozine method for quantitative assay of mineral systems for ferrous and total iron. *Geochimica et Cosmochimica Acta*, **72**, 5001–5008.

Bazylinski, D.A. and Frankel, R.B. (2003) Biologically controlled mineralization in prokaryotes. Pp. 217–247 in: *Biomineralization* (P.M. Dove, J.J. DeYoreo, and S. Weiner, editors). Reviews in Mineralogy and Geochemistry, **54**, Mineralogical Society of America, Chantilly, Virginia and The Geochemical Society.

Benzerara, K. and Menguy, N. (2009) Looking for traces of life in minerals. *Comptes Rendus Palevol*, **8**, 617–628.

Buatier, M.D., Guillaume, D., Wheat, C.G., Hervé, L., and Adatte, T. (2004) Mineralogical characterization and genesis of hydrothermal Mn oxides from the flank of the Juan the Fuca Ridge. *American Mineralogist*, **89**, 1807–1815

Childers, S.E., Ciufo, S., and Lovley, D.R. (2002) Geobacter metallireducens accesses insoluble Fe(III) oxide by chemotaxis. *Nature*, **416**, 767–769.

Daulton, T.L., Little, B.J., Lowe, K., and Jones-Meehan, J. (2002) Electron energy loss spectroscopy techniques for the study of microbial chromium(VI) reduction. *Journal of Microbiological Methods*, **50**, 39–54.

Daulton, T.L., Little, B.J., Jones-Meehan, J., Blom D.A., and Allard, L.F. (2007) Microbial reduction of chromium from the hexavalent to divalent state. *Geochimica et Cosmochimica Acta*, **71**, 556–565.

Dong, H., Fredrickson, J.K., Kennedy, D.W., Zachara, J.M., Kukkadapu, R.K., and Onstott, T.C. (2000) Mineral transformation associated with the microbial reduction of magnetite. *Chemical Geology*, **169**, 299–318.

Dong, H., Jaisi, D.P., Kim, J.W., and Zhang, G. (2009) Microbe–clay mineral interactions: A Review. *American Mineralogist*, **94**, 1505–1519.

Dyar, M.D., Solberg, T.C., and Burns, R.G. (1986) The effects

of composition, oxygen fugacity, and crystal structure on the color of hibonite. *Lunar and Planetary Science*, **17**, 194–195.

Eberl, D.D., Nüesch, R., Sucha, V., and Tsipursky, S. (1998) Measurement of fundamental illite particle thicknesses by X-ray diffraction using PVP-10 intercalation. *Clays and Clay Minerals*, **46**, 89–97.

Elliott, J.C. (2002) Calcium phosphate biominerals. Pp. 427–453 in: *Phosphates: Geochemical, Geobiological, and Materials Importance* (J.M. Kohn, J. Rakovan, and J.M. Hughes, editors). Reviews in Mineralogy and Geochemistry, **48**, Mineralogical Society of America, Washington, D.C. and the Geochemical Society.

Fredrickson, J.K., Zachara, J.M., Kennedy, D.W., Dong, H., Onstott, T.C., Hinman, N.W., and Li, S.M. (1998) Biogenic iron mineralization accompanying the dissimilatory reduction of hydrous ferric oxide by a groundwater bacterium. *Geochimica et Cosmochimica Acta*, **62**, 3239–3257.

Garvie, L.A.J., Craven, A.J., and Brydson, R. (1994) Use of electron-loss near-edge fine structure in the study of minerals. *American Mineralogist*, **79**, 411–425.

Garvie, L.A.J., Zega, T.J., Rez, P., and Buseck, P.R. (2004) Nanometer-scale measurements of Fe^{3+}/ ΣFe by electron energy-loss spectroscopy: a cautionary note. *American Mineralogist*, **89**, 1610–1616.

Golla, U. and Putnis, A. (2001) Valence state mapping and quantitative electron spectroscopic imaging of exsolution in titanohematite by energy-filtered TEM. *Physics and Chemistry of Minerals*, **28**, 119–129.

Hunt, J.A. and Williams, D.B. (1991) Electron energy-loss spectrum imaging. *Ultramicroscopy*, **38**, 47–73.

Jaisi, D.P., Dong, H., and Liu, C. (2007) Influence of biogenic Fe(II) on the extent of microbial reduction of Fe(III) in clay minerals nontronite, illite, and chlorite. *Geochimica et Cosmochimica Acta*, **71**, 1145–1158.

Kim, J.W., Peacor, D.R., Tessier, D., and Elsass, F. (1995) A technique for maintaining texture and permanent expansion of smectite interlayers for TEM observations. *Clays and Clay Minerals*, **43**, 51–57.

Kim, J.W., Furukawa, Y., Daulton, T.L., Lavoie, D., and Newell, S.W. (2003) Characterization of microbially Fe (III)-reduced nontronite: environmental cell-transmission electron microscopy study. *Clays and Clay Minerals*, **51**, 382–389.

Kim, J.W., Dong, H., Seabaugh, J., Newell, S.W., and Eberl, D.D. (2004) Role of microbes in the smectite-to-illite reaction. *Science*, **303**, 830–832.

Konhouser, K.O. (1998) Diversity of bacterial iron mineralization. *Earth-Science Reviews*, **43**, 91–121.

Konhauser, K.O. and Ferris, F.G. (1996) Diversity of iron and silica precipitation by microbial biofilms in hydrothermal waters, Iceland: implications for Precambrian Iron Formations. *Geology*, **24**, 323–326.

Konhauser, K.O., Jones, B., Phoenix, V.R., Ferris, G., and Renaut, R.W. (2004) The microbial role in hot spring silicification. *Ambio*, **33**, 552–558.

Kostka, J.E. and Nealson, K.H. (1995) Dissolution and Reduction of magnetite by bacteria. *Environmental Science & Technology*, **29**, 2535–2540.

Kostka, J.E., Haefele, E., Viehwegar, R., and Stuki, J.W. (1999) Respiration and dissolution of iron(III)-containing clay minerals by bacteria. *Environmental Science & Technology*, **33**, 3127–3133.

Kukkadapu, R.K., Zachara, J.M., Smith, S.C., Fredrickson, J.K., and Liu, C.X. (2001) Dissimilatory bacterial reduction of Al-substituted goethite in subsurface sediments. *Geochimica et Cosmochimica Acta*, **65**, 2913–2924.

Leapman, R.D. and Sywt, C.R. (1988) Separation of overlapping core edges in electron energy loss spectra by multiple-least-squares fitting. *Ultramicroscopy*, **26**, 393–403.

Leapman, R.D., Grunes, L.A. and Fejes, P.L. (1982) Study of the L_{23} edges in the 3d transition metals and their oxides by electron-energy-loss spectroscopy with comparisons to theory. *The American Physical Society*, **26**, 614–635.

Leppard, G.G., Heissenberger, A., and Herndl, G.J. (1996) Ultrastructure of marine snow. I. Transmission electron microscopy methodology. *Marine Ecology Progress Series*, **135**, 289–298.

Li, Y.L., Zhang, C.L., Yang, J., Deng, B., and Vali, H. (2004) Iron reduction and alteration of nontronite NAu-2 by a sulfate-reducing bacterium. *Geochimica et Cosmochimica Acta*, **68**, 3251–3260.

Liu, C., Kota, S., Zachara, J.M., Fredrickson, J.K., and Brinkman, C.K. (2001) Kinetic analysis of the bacterial reduction of goethite. *Environmental Science & Technology*, **35**, 2482–2490.

Lovley, D.R., Coates, J.D., Woodward, J.C., and Phillips, E.J.P. (1995) Benzene oxidation coupled to sulfate reduction. *Applied and Environmental Microbiology*, **61**, 953–958.

Middleton, S.S., Latmani, R.B., Mackey, M.R., Ellisman, M.H., Tebo, B.M., and Criddle, C.S. (2003) Cometabolism of Cr(VI) by *Shewanella oneidensis* MR-1 produces cell-associated reduced chromium and inhibits growth. *Biotechnology and Bioengeineering*, **83**, 627–637.

Nealson, K.H. and Little, B. (1997) Breathing manganese and iron: solid-state respiration. *Advances in Applied Microbiology*, **45**, 213–239.

Nealson, K.H. and Saffarini, D. (1994) Iron and manganese in anaerobic respiration: environmental significance, physiology, and regulation. *Annual Reviews in Microbiology*, **48**, 311–343.

Nevin, K.P. and Lovley, D.R. (2002) Mechanisms for Fe(III) oxide reduction in sedimentary environments. *Geomicrobiological Journal*, **19**, 141–159.

Newman, D.K. and Kolter, R. (2000) A role for excreted quinones in extracellular electron transfer. *Nature*, **405**, 93–97.

Paterson, J.H. and Krivanek, O.L. (1990) ELNES of 3d transition-metal oxides, II. Variations with oxidation state and crystal structure. *Ultramicroscopy*, **32**, 319.

Roden, E.E. and Zachara, J.M. (1996) Microbial reduction of crystalline Fe(III) oxides: influence of oxide surface area and potential for cell growth. *Environmental Science & Technology*, **30**, 1618–1628.

Taftø, J. and Krivanek, O.L. (1982) Site-specific valence determination by electron energy-loss spectroscopy. *Physical Review Letters*, **48**, 560–563.

Tazaki, K. and Asada, R. (2001) Microbes associated with clay minerals: formation of bio-halloysite. Pp. 569–576 in: *A Clay Odyssey* (E.A. Dominguez, G.R. Mas, and F. Cravero, editors). Elsevier, Amsterdam.

Tazaki, K. and Asada, R. (2007) Transmission electron microscopic observation of mercury-bearing bacterial clay minerals in a small-scale gold mine in Tanzania. *Geobicrobiology Journal*, **24**, 477–489.

van Aken, P.A. and Liebscher (2002) Quantification of ferrous/ferric ratios in minerals: new evaluation schemes of Fe L23 electron ecergy-loss near-edge spectra. *Physics and Chemistry of Minerals*, **29**, 188–200.

van Aken, P.A., Liebscher, B., and Styrsa, V.J. (1998) Quantitative determination of iron oxidation states in minerals using Fe L-2,L-3-edge electron energy-loss near-edge structure spectroscopy. *Physics and Chemistry of Minerals*, **25**, 323–327.

van Aken, P.A., Styrsa, V.J., Liebscher, B., Woodland, A.B., and Redhammer, G.J. (1999) Microanalysis of Fe^{3+}/ΣFe in

oxide and silicate minerals by investigation of electron energy-loss near-edge structures (ELNES) at the Fe M2,3 edge. *Physics and Chemistry of Minerals*, **26**, 574–590.

Weiner, S. and Dove, P.M. (2003) An overview of biomineralization processes and the problem of the vital effects. Pp. 1–24 in: *Biomineralization* (P.M. Dove, J.J. de Yoreo, and S. Weiner, editors). Reviews in Mineralogy, **54**, Mineralogical Society of America, Chantilly, Virginia, USA, and the Geochemical Society.

Zhang, S., Livi, K.J.T., Gaillot, A., Stone, A.T. and Veblen, D.R. (2010) Determination of manganese valence state in (Mn^{3+}, Mn^{4+}) minerals by electron energy loss spectroscopy. *American Mineralogist*, **95**, 1741–1746.

(*Received 18 August 2010; revised 14 February 2011; Ms. 473; A.E. L.B. Williams*)